Non-Markovian heat production in ultrafast phonon dynamics

Fredrik Eriksson,[1] Yulong Qiao,[1,*] Erik Fransson,[1] R. Matthias Geilhufe,[1,†] and Paul Erhart[1,‡]

[1] *Department of Physics, Chalmers University of Technology, SE-41296, Gothenburg, Sweden*

(Dated: March 9, 2026)

High-intensity THz laser pulses enable the light-mediated control of lattice vibrations by resonantly driving selected phonon modes. On ultrafast timescales, memory effects influence the phonon dynamics and must be accounted for to describe the heat production associated with energy dissipation. Here, we establish a microscopic framework for non-Markovian phonon dynamics by deriving the noise and dissipation kernels governing a driven phonon mode. Using large-scale molecular dynamics simulations, we reconstruct these kernels directly from the many-body lattice dynamics and determine the corresponding heat production rate. Our results provide a quantitative picture of the crossover between Markovian and non-Markovian dynamics on picosecond timescales and show how the finite bandwidth of the driving field limits the dynamically relevant bath spectrum. Furthermore, we demonstrate that thermodynamic quantities such as heat production can be inferred directly from the dynamics of an individual phonon mode, enabling their experimental measurement using time-resolved spectroscopy.

Intense THz laser pulses enable the selective excitation and coherent control of optical phonon modes [1–3]. Driving the lattice along specific vibrational coordinates has opened nonthermal pathways to metastable phases [4–10], phonon-induced magnetism [11–23], and ultrafast magnetic switching [24, 25]. These advances raise a fundamental question: how is heat produced when a solid is driven far from equilibrium on picosecond timescales?

Recent theoretical work has begun to frame laser-driven phonons within stochastic thermodynamics, highlighting the interplay of fluctuations and dissipation in generating heat and entropy [26–28]. In such descriptions, the driven mode acts as a subsystem coupled to an effective bath formed by the remaining lattice degrees of freedom. Energy transfer from coherent motion into this bath enhances fluctuations and results in entropy production. However, the microscopic structure of this bath and the validity of Markovian assumptions under strong driving remain largely unexplored.

Here we establish a microscopic framework for ultrafast thermodynamics that resolves heat production at the level of individual phonon modes. By combining large-scale molecular dynamics (MD) simulations with a mode-resolved theoretical description, we obtain deterministic access to the full many-body lattice dynamics and project it onto normal-mode coordinates. This approach enables a direct and quantitative comparison between atomistic simulations and stochastic effective theories. From this comparison we derive a non-Markovian Langevin equation for a laser-driven phonon mode and identify the microscopic origin of memory effects in terms of mode–mode coupling.

We show that far-from-equilibrium driving generates a highly structured effective bath whose spectral density is dominated by discrete phonon modes rather than a continuum. Despite this structure, a Markovian approximation can remain quantitatively accurate once the finite frequency resolution of the driving field is taken into account. Our results clarify when simplified stochastic descriptions capture ultrafast heat production and when genuinely non-Markovian effects become essential.

As a concrete realization we consider the ferroelectric soft mode of the perovskite STO, a prototypical quantum paraelectric with strongly anharmonic lattice dynamics [9, 18, 26, 29]. Its proximity to structural instability and pronounced temperature-dependent softening make it an ideal platform for exploring nonequilibrium phonon thermodynamics (Supp. Note 1) [30–34]. While the material serves as a representative example, the framework developed here is general and applicable to driven lattice systems more broadly.

To capture the interplay of lattice instabilities, fluctuations, and dissipation beyond harmonic models, we employ a machine-learned interatomic potential (MLIP) trained within the neuroevolution potential (NEP) framework [35–38] as an efficient emulator of density functional theory (DFT) calculations [39–41] using the van-der-Waals density functional with consistent exchange [42, 43]. This description accurately reproduces the relevant lattice dynamics and anharmonic couplings governing energy redistribution. To investigate the nonequilibrium dynamics of the ferroelectric soft mode following optical excitation, and to analyze the associated dissipation mechanisms and thermodynamic changes, we performed a large ensemble of MLIP-MD simulations. In these simulations, the laser pulse was modeled as an effective time-dependent driving force $F_{\mathrm{L}}(t)$ acting directly on the soft-mode amplitude,

$$F_{\mathrm{L}}(t) = \beta Z E \exp\left(-\frac{1}{2}\frac{(t-t_0)^2}{\tau^2}\right)\cos\left(\omega_{\mathrm{L}} t\right). \qquad (1)$$

Here, Z denotes the mode effective charge [44], which is $Z \approx 1.2\,\mathrm{e}^{+}/\sqrt{\mathrm{Da}}$ (see Supp. Note 8), and β accounts for the screening of the electric field within the sample, approximated as $\beta = 0.215$ [29]. We used a force amplitude of $22.2\,\sqrt{\mathrm{Da}}\mathrm{\AA}/\mathrm{ps}^2$, corresponding to an elec-

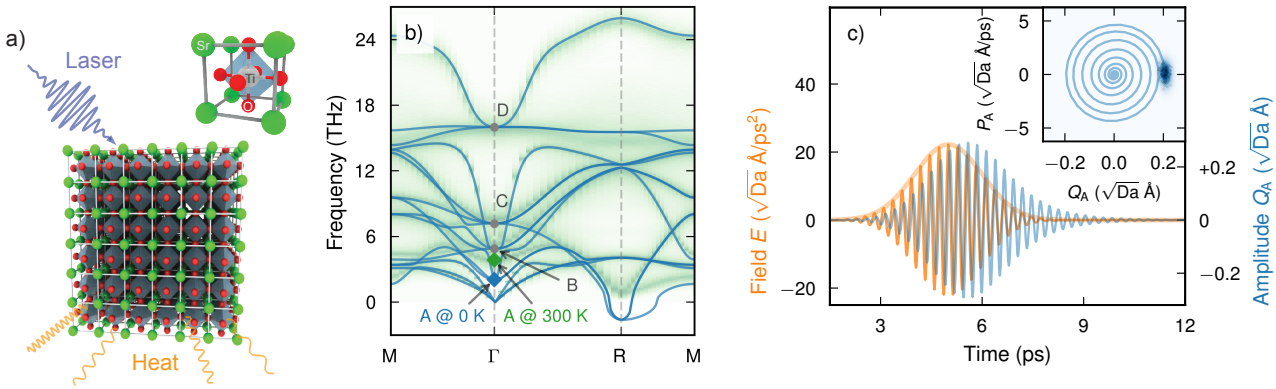

FIG. 1. (a) Schematic illustrating of STO driven by a THz laser pulse, leading to pumping of the ferroelectric mode, which on decay leads to the ultrafast generation of heat. The inset shows the primitive unit cell. (b) Phonon band structure along a high-symmetry path through the Brillouin zone. Solid blue lines show the harmonic dispersion corresponding to the zero-temperature limit. The green color map shows the spectral energy density representing the dispersion at 300 K. The ferroelectric mode (marked A), has a pronounced temperature dependence. The other Γ-modes are labeled B through D (see Fig. S3 for a more explicit illustration of their temperature dependence). (c) Excitation field due to the laser (in orange; with envelope indicated) and the mode amplitude of the ferroelectric mode (in blue) as a function of time. The inset shows the sampling of the phase space of the driven mode as a kernel-density map over the distribution of trajectories with markers representing specific simulations at approximately 5.59 ps corresponding to the maximum amplitude. The line shows the average path through phase space up to this time.

tric field of $E \approx 860\,\mathrm{kV\,cm^{-1}}$, comparable to values employed in recent experiments [2, 18, 20, 25, 29]. The pulse duration was set to $\tau = 1\,\mathrm{ps}$ with its peak centered at $t_0 = 5\,\mathrm{ps}$ (Fig. 1c), and the central frequency $\omega \approx 3.66\,\mathrm{THz}$ was chosen close to resonance with the computed room-temperature soft-mode frequency of approximately 3.84 THz (Table S1).

We obtain the time-dependent mode coordinates $Q_\lambda(t)$ for a phonon mode $\lambda = (\mathbf{k}, n)$ by projecting each MD configuration onto the corresponding phonon eigenvectors [45–47]. For the ferroelectric soft mode at the Γ point, $Q_\mathrm{A} = Q_{\mathbf{0},1}$, this projection yields

$$Q_\mathrm{A} = \frac{1}{\sqrt{N_c}} \sum_{\nu,\alpha} \sqrt{m_\nu}\, \mathbf{e}^A_{\nu\alpha}\, \tau^A_{\nu\alpha}, \tag{2}$$

where N_c is the number of unit cells and $\mathbf{e}^A_{\nu\alpha}$ denotes the normalized eigenvector of the soft mode at Γ, with ν and α labeling atomic species and Cartesian direction, respectively. Here, m_ν is the atomic mass and $\tau^A_{\nu\alpha}$ the Fourier component of the atomic displacement at the Γ-point. The mass-weighted mode coordinate Q_A thus has units of $\sqrt{\mathrm{Da}}\,\mathrm{Å}$.

The laser excitation drives the soft mode to a maximum amplitude of almost $0.3\,\sqrt{\mathrm{Da}}\mathrm{Å}$ (blue line in Fig. 1c). Because the pulse duration (1 ps) exceeds the oscillation period of the mode, several coherent oscillations occur during the driving. However, the strong damping of the ferroelectric soft mode limits its lifetime to a timescale comparable to the pulse duration, and the amplitude rapidly relaxes toward equilibrium once the driving field vanishes. This pronounced damping reflects the energy transfer from the driven mode to the surrounding lattice degrees of freedom.

To interpret the phonon dynamics and associated energy transfer processes observed in the MD simulations, we formulate an ultrafast stochastic thermodynamic framework based on a classical phonon–bath coupling model. A full quantum mechanical treatment is discussed in Ref. [27]. Here we focus on the classical limit appropriate for the large-amplitude, finite-temperature dynamics considered in this work. We partition the phonon system into the driven ferroelectric soft mode and an effective bath comprising all remaining lattice degrees of freedom, and describe their coupled dynamics by the classical Lagrangian [48],

$$\mathcal{L} = \frac{\dot{Q}_\mathrm{A}^2}{2} - \frac{1}{2}\omega_\mathrm{A}^2 Q_\mathrm{A}^2 + F_\mathrm{L}(t) Q_\mathrm{A} + \sum_{i=1} \left[\frac{\dot{Q}_i^2}{2} - \frac{\omega_i^2}{2} \left(Q_i - \frac{\kappa_i}{\omega_i^2} Q_\mathrm{A} \right)^2 \right]. \tag{3}$$

Here, $Q_\mathrm{A}(t)$ denotes the amplitude of the ferroelectric mode defined in Eq. (2), $\dot{Q}_\mathrm{A}(t)$ its generalized velocity, and ω_A its angular frequency. The laser force $F_\mathrm{L}(t)$ is given by Eq. (1). The bath is represented by a large set of harmonic modes indexed by i. Although real phonon–phonon interactions involve anharmonic couplings of various polynomial orders, a linear mode–bath coupling term $\kappa_i Q_\mathrm{A} Q_i$ provides an effective description of dissipation and energy transfer from the soft mode at the level of coarse-grained dynamics.

Eliminating the bath degrees of freedom yields the effective equation of motion for the soft mode (see Supp.

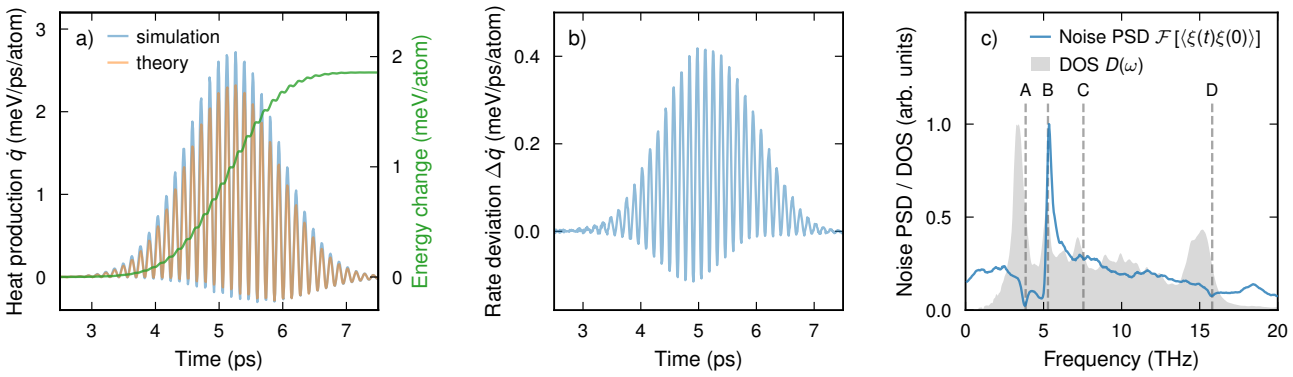

FIG. 2. (a) Total energy and heat production rate $\dot{q}(t)$ during pulse, where $\dot{q}(t)$ is obtained as the time derivative of the total energy. (b) Deviation in heat production rate between simulation and theory. (c) Noise PSD $\mathcal{F}[\langle\xi(t)\xi(0)\rangle]$ of the ferroelectric mode (A in Fig. 1b) in comparison with the density of states (DOS). The vertical dashed lines indicate the frequencies of the Γ-point modes (see Fig. S4 for the noise PSDs for all modes).

Note 9 for details),

$$\ddot{Q}_{\mathrm{A}} + \omega_{\mathrm{A}}^2 Q_{\mathrm{A}} + \int_{-\infty}^{t} \mathrm{d}s\, f(t-s)\, \dot{Q}_{\mathrm{A}}(s) = F_{\mathrm{L}}(t) + \xi_{\mathrm{A}}(t), \tag{4}$$

which takes the form of a generalized Langevin equation. Dissipation is governed by the memory kernel $f(t)$ through the convolution term, where

$$f(t) = \int_0^{\infty} \mathrm{d}\omega\, D(\omega) \frac{\kappa^2(\omega)}{\omega^2} \cos(\omega t), \tag{5}$$

and depends on the phonon density of states $D(\omega)$ and the mode–bath coupling strength $\kappa(\omega)$. The stochastic force $\xi(t)$ is a Gaussian colored noise with correlation function $\eta(t) = \langle\xi(t)\xi(0)\rangle$ satisfying the classical fluctuation–dissipation theorem in the Fourier domain,

$$\mathcal{F}[\eta(t)] = k_{\mathrm{B}} T\, \mathcal{F}[f(t)], \tag{6}$$

where $\mathcal{F}[\cdots]$ denotes the Fourier transform. The quantity $\mathcal{F}[\eta(t)]$ corresponds to the power spectral density (PSD) of the stochastic force and, according to Eq. (5) and Eq. (6), is proportional to $D(\omega)\kappa^2(\omega)/\omega^2$ up to a temperature factor.

The generalized Langevin equation (4) describes non-Markovian dynamics due to the memory kernel entering through the convolution term. In practice, however, the kernel $f(t)$ can often not be directly accessed from simulations or experiments. If $f(t)$ can be approximated as time-local, the equation of motion reduces to

$$\ddot{Q}_{\mathrm{A}} + \omega_{\mathrm{A}}^2 Q_{\mathrm{A}} + \gamma_{\mathrm{A}} \dot{Q}_{\mathrm{A}} = F_{\mathrm{L}}(t) + \xi_{\mathrm{A}}(t), \tag{7}$$

where γ_{A} denotes the damping rate and ω_{A} the renormalized soft-mode frequency. In this limit, $Q_{\mathrm{A}}(t)$ follows Markovian dynamics [26].

To extract the stochastic force $\xi_{\mathrm{A}}(t)$ from the MD simulations, we project the atomic forces (excluding the laser force $F_{\mathrm{L}}(t)$) onto the phonon eigenmodes (Supp. Note 6). For the modes at Γ, including the ferroelectric soft mode A, we perform a least-squares fit of the total mode force to the form $\omega_\lambda^2 Q_\lambda(t) + \gamma_\lambda \dot{Q}_\lambda(t)$ to determine the renormalized frequencies ω_λ and damping rates γ_λ. Frequency shifts induced by anharmonic interactions are thus absorbed into ω_λ, while energy dissipation into other modes is captured by γ_λ. The stochastic force $\xi_\lambda(t)$ is identified as the residual after subtracting the harmonic and friction contributions. After this fitting procedure, the dynamics of the soft mode coordinate ($Q_A(t)$ in Fig. 1c) is fully captured by the time-local Langevin equation Eq. (7), upon averaging over the zero-mean stochastic force. The parameters are given by the soft mode frequency $\omega_A = 3.84\,\mathrm{THz}$ and the soft mode damping $\gamma_A = 0.35\,\mathrm{THz}$ (Table S1).

The increase in the total energy of the system, $\Delta E(t)$, relative to its pre-pulse value can be interpreted as the net heat deposited into the lattice due to the work performed by the laser. This energy change can be written as an integral over the heat production rate $\dot{q}(t)$,

$$\Delta E(t) = \int_{-\infty}^{t} \mathrm{d}\tau\, \dot{q}(\tau). \tag{8}$$

In the MD simulations, $\Delta E(t)$ is obtained by summing the kinetic and potential energies of all atoms (green line in Fig. 2a). The total energy increases rapidly during the pump and saturates shortly after the pulse, indicating that the energy deposition process is essentially completed within 3 ps. The instantaneous heat production rate $\dot{q}(t)$ is computed as the time derivative of the total energy. It oscillates during the pulse and reaches a maximum near 5 ps, consistent with the soft-mode dynamics (blue line in Fig. 1c). The small negative contribution

around 6 ps arises from the slight frequency mismatch between the laser and the soft mode.

Within the stochastic thermodynamic description based on on the generalized Langevin equation (4), the heat production rate can be evaluated analytically. At the level of a single trajectory, the time derivative of the internal energy $U_{\mathrm{A}}(t)$ of the soft mode is given by

$$\dot{U}_{\mathrm{A}}(t) = F_{\mathrm{L}}(t)\dot{Q}_{\mathrm{A}}(t) + \Delta\dot{Q}. \tag{9}$$

The first term represents the work rate performed by the laser on the soft mode. The second term quantifies the stochastic energy flux from the thermal bath into the soft mode,

$$\Delta\dot{Q} = \left[\xi_A(t) - \int_{-\infty}^{t} \mathrm{d}s\, f(t-s)\, \dot{Q}_{\mathrm{A}}(s)\right] \circ \dot{Q}_{\mathrm{A}}. \tag{10}$$

Here, $\circ$ denotes the Stratonovich product [49]. Taking the ensemble average and using the first-law relation, the heat production rate becomes

$$\dot{q}(t) = \left\langle \dot{U}_{\mathrm{A}}(t) - \Delta\dot{Q}(t) \right\rangle = \left\langle F_{\mathrm{L}}(t)\dot{Q}_{\mathrm{A}}(t) \right\rangle, \tag{11}$$

where $\langle \cdots \rangle$ denotes the ensemble average over stochastic trajectories. The heat production rate is therefore determined by the correlation between the laser force and the velocity of the driven phonon mode.

The form of Eq. (11) is general, while non-Markovian effects enter through the dynamics of $Q_A(t)$ governed by the generalized Langevin equation Eq. (4) with memory kernel $f(t)$. Using the Markovian approximation Eq. (7) together with Eq. (11) yields the theoretical prediction shown as the orange line in Fig. 2a. Comparison with the MD result (blue line) shows very good agreement, although the theory slightly overestimates the peak value (Fig. 2b). This agreement confirms that the stochastic thermodynamic description captures the essential mechanisms governing energy transfer during ultrafast lattice excitation.

To shed light into the form of the actual memory kernel $f(t)$ we compute the PSD of the zero-mean stochastic forces using the Fourier transform of the autocorrelation function $\langle \xi(t)\xi(0) \rangle$. By construction, the PSD vanishes at the respective eigenfrequency of each mode. The PSDs are clearly non-uniform, demonstrating that the effective noise is colored (Fig. 2c; Fig. S4). Comparison of the PSD for the ferroelectric soft mode A with the phonon density of states $D(\omega)$ shows that the spectral structure does not simply follow $D(\omega)$, highlighting the role of the coupling strength $\kappa(\omega)$. In particular, the PSD for mode A exhibits a pronounced peak at $\omega_{\mathrm{B}} = 5.26\,\mathrm{THz}$, revealing strong coupling to mode B. Applying the same analysis to the remaining Γ-point modes shows a much weaker coupling to mode D and no observable coupling to mode C, consistent with modes A and C belonging to different symmetry representations (see Table S1). Similar spectral features have previously been observed in time-resolved X-ray scattering experiments [29].

The structured PSD indicates a nonlocal friction kernel and thus, in principle, non-Markovian dynamics according to Eq. (6). However, the observed soft-mode dynamics is well captured by the Markovian equation Eq. (7). This apparent discrepancy can be understood by considering the finite frequency resolution of the laser pulse. The driven response of the mode is governed by the product of the frequency response function $\chi(\omega)$ defined in Supp. Note 9 and the spectral profile of the driving field $F_{\mathrm{L}}(\omega)$. Because the pulse duration $\tau = 1\,\mathrm{ps}$ is much longer than the soft-mode period, the spectrum of the driving field is narrowly peaked around ω_{L}. Within this restricted frequency window, the response function varies only weakly and can be approximated by its local expansion, effectively yielding a constant damping rate γ. As a result, the non-Markovian dynamics reduces to an effective Markovian form on the timescale set by the pulse. For shorter pulses with broader spectral bandwidth, deviations from Markovian behavior are expected to become observable, as illustrated in [27].

In conclusion, we have developed a microscopic framework to quantify non-Markovian heat production in ultrafast phonon dynamics by integrating large-scale MD simulations with a stochastic, mode-resolved theoretical description. Using a MLIP with near–DFT accuracy, we resolved the full many-body lattice dynamics of a realistic solid, projected them onto phonon normal modes, and reconstructed the structured effective bath governing a laser-driven phonon mode. This approach establishes a direct bridge between deterministic atomistic simulations and stochastic thermodynamics, enabling the extraction of memory kernels and bath spectral densities from first principles.

The resulting generalized Langevin description quantitatively reproduces the ultrafast dynamics observed in the simulations and reveals strongly mode-selective energy transfer within the lattice. We show that the heat production rate can be inferred directly from the driven-mode dynamics, yielding excellent agreement with the fully atomistic simulations. Our analysis further demonstrates that far-from-equilibrium driving generates a highly structured bath with a non-uniform PSD, reflecting discrete phonon couplings rather than a featureless continuum. Nevertheless, the finite frequency bandwidth of the driving pulse limits the dynamically relevant spectral window, such that an effective Markovian description remains accurate on picosecond timescales.

While illustrated here for the ferroelectric soft mode of STO, the framework is general and applicable to driven lattice systems beyond this specific material realization. Our results provide a quantitative and mode-resolved understanding of how dissipation, heat production, and fluctuations emerge in strongly driven

solids. More broadly, this work establishes a route toward first-principles-informed ultrafast thermodynamics, where non-Markovian effects can be identified, quantified, and systematically explored in experiments on quantum materials.

DATA AVAILABILITY

The DFT data and NEP model generated in this study are openly available via Zenodo at `https://doi.org/10.5281/zenodo.18841778`.

* yulong.qiao@chalmers.se
† matthias.geilhufe@chalmers.se
‡ erhart@chalmers.se

[1] A. S. Disa, T. F. Nova, and A. Cavalleri, Nature Physics **17**, 1087 (2021).
[2] P. Salén, M. Basini, S. Bonetti, J. Hebling, M. Krasilnikov, A. Y. Nikitin, G. Shamuilov, Z. Tibai, V. Zhaunerchyk, and V. Goryashko, Physics Reports **836-837**, 1 (2019).
[3] D. Nicoletti and A. Cavalleri, Advances in Optics and Photonics **8**, 401 (2016).
[4] D. Fausti, R. I. Tobey, N. Dean, S. Kaiser, A. Dienst, M. C. Hoffmann, S. Pyon, T. Takayama, H. Takagi, and A. Cavalleri, Science **331**, 189 (2011).
[5] A. Subedi, Physical Review B **95**, 134113 (2017).
[6] T. F. Nova, A. S. Disa, M. Fechner, and A. Cavalleri, Science **364**, 1075 (2019).
[7] M. Buzzi, D. Nicoletti, S. Fava, G. Jotzu, K. Miyagawa, K. Kanoda, A. Henderson, T. Siegrist, J. A. Schlueter, M.-S. Nam, A. Ardavan, and A. Cavalleri, Physical Review Letters **127**, 197002 (2021).
[8] M. Budden, T. Gebert, M. Buzzi, G. Jotzu, E. Wang, T. Matsuyama, G. Meier, Y. Laplace, D. Pontiroli, M. Riccò, F. Schlawin, D. Jaksch, and A. Cavalleri, Nature Physics **17**, 611 (2021).
[9] S. Latini, D. Shin, S. A. Sato, C. Schäfer, U. D. Giovannini, H. Hübener, and A. Rubio, Proceedings of the National Academy of Sciences **118**, 10.1073/pnas.2105618118 (2021).
[10] B. Cheng, P. L. Kramer, Z.-X. Shen, and M. C. Hoffmann, Physical Review Letters **130**, 126902 (2023).
[11] D. M. Juraschek, M. Fechner, A. V. Balatsky, and N. A. Spaldin, Physical Review Materials **1**, 014401 (2017).
[12] D. M. Juraschek and N. A. Spaldin, Physical Review Materials **3**, 064405 (2019).
[13] B. Cheng, T. Schumann, Y. Wang, X. Zhang, D. Barbalas, S. Stemmer, and N. P. Armitage, Nano Letters **20**, 5991 (2020).
[14] R. M. Geilhufe, V. Juričić, S. Bonetti, J.-X. Zhu, and A. V. Balatsky, Physical Review Research **3**, L022011 (2021).
[15] Y. Ren, C. Xiao, D. Saparov, and Q. Niu, Physical Review Letters **127**, 186403 (2021).
[16] D. M. Juraschek, T. Neuman, and P. Narang, Physical Review Research **4**, 013129 (2022).
[17] A. Baydin, F. G. G. Hernandez, M. Rodriguez-Vega, A. K. Okazaki, F. Tay, G. T. Noe, I. Katayama, J. Takeda, H. Nojiri, P. H. O. Rappl, E. Abramof, G. A. Fiete, and J. Kono, Physical Review Letters **128**, 075901 (2022).
[18] M. Basini, M. Pancaldi, B. Wehinger, M. Udina, V. Unikandanunni, T. Tadano, M. C. Hoffmann, A. V. Balatsky, and S. Bonetti, Nature **628**, 534 (2024).
[19] R. M. Geilhufe and W. Hergert, Physical Review B **107**, L020406 (2023).
[20] J. Luo, T. Lin, J. Zhang, X. Chen, E. R. Blackert, R. Xu, B. I. Yakobson, and H. Zhu, Science **382**, 698 (2023).
[21] F. G. G. Hernandez, A. Baydin, S. Chaudhary, F. Tay, I. Katayama, J. Takeda, H. Nojiri, A. K. Okazaki, P. H. O. Rappl, E. Abramof, M. Rodriguez-Vega, G. A. Fiete, and J. Kono, Science Advances **9**, eadj407 (2023).
[22] N. Shabala and R. M. Geilhufe, Physical Review Letters **133**, 266702 (2024).
[23] N. Shabala, F. Tietjen, and R. M. Geilhufe, arXiv:2511.03329 (2025).
[24] A. S. Disa, M. Fechner, T. F. Nova, B. Liu, M. Först, D. Prabhakaran, P. G. Radaelli, and A. Cavalleri, Nature Physics **16**, 937 (2020).
[25] C. S. Davies, F. G. N. Fennema, A. Tsukamoto, I. Razdolski, A. V. Kimel, and A. Kirilyuk, Nature **628**, 540 (2024).
[26] L. Caprini, H. Löwen, and R. M. Geilhufe, Nature Communications **15**, 94 (2024).
[27] Y. Qiao and R. M. Geilhufe, arXiv:2512.17669 (2025).
[28] F. Tietjen and R. M. Geilhufe, PNAS Nexus **4** (2025).
[29] M. Kozina, M. Fechner, P. Marsik, T. van Driel, J. M. Glownia, C. Bernhard, M. Radovic, D. Zhu, S. Bonetti, U. Staub, and M. C. Hoffmann, Nature Physics **15**, 387 (2019).
[30] P. A. Fleury, J. F. Scott, and J. M. Worlock, Physical Review Letters **21**, 16 (1968).
[31] R. A. Cowley, Philosophical Transactions of the Royal Society of London. Series A: Mathematical, Physical and Engineering Sciences **354**, 2799 (1996).
[32] M. Holt, M. Sutton, P. Zschack, H. Hong, and T.-C. Chiang, Physical Review Letters **98**, 065501 (2007).
[33] K. A. Müller and H. Burkard, Physical Review B **19**, 3593 (1979).
[34] C. Verdi, L. Ranalli, C. Franchini, and G. Kresse, Physical Review Materials **7**, L030801 (2023).
[35] Z. Fan, Y. Wang, P. Ying, K. Song, J. Wang, Y. Wang, Z. Zeng, K. Xu, E. Lindgren, J. M. Rahm, A. J. Gabourie, J. Liu, H. Dong, J. Wu, Y. Chen, Z. Zhong, J. Sun, P. Erhart, Y. Su, and T. Ala-Nissila, The Journal of Chemical Physics **157**, 114801 (2022).
[36] K. Xu, H. Bu, S. Pan, E. Lindgren, Y. Wu, Y. Wang, J. Liu, K. Song, B. Xu, Y. Li, T. Hainer, L. Svensson, J. Wiktor, R. Zhao, H. Huang, C. Qian, S. Zhang, Z. Zeng, B. Zhang, B. Tang, Y. Xiao, Z. Yan, J. Shi, Z. Liang, J. Wang, T. Liang, S. Cao, Y. Wang, P. Ying, N. Xu, C. Chen, Y. Zhang, Z. Chen, X. Wu, W. Jiang, E. Berger, Y. Li, S. Chen, A. J. Gabourie, H. Dong, S. Xiong, N. Wei, Y. Chen, J. Xu, F. Ding, Z. Sun, T. Ala-Nissila, A. Harju, J. Zheng, P. Guan, P. Erhart, J. Sun, W. Ouyang, Y. Su, and Z. Fan, Materials Genome Engineering Advances **3**, e70028 (2025).
[37] E. Lindgren, M. Rahm, E. Fransson, F. Eriksson, N. Österbacka, Z. Fan, and P. Erhart, Journal of Open

Source Software **9**, 6264 (2024).
[38] T. Schaul, T. Glasmachers, and J. Schmidhuber, in *Proceedings of the 13th Annual Conference on Genetic and Evolutionary Computation*, GECCO '11 (Association for Computing Machinery, New York, NY, USA, 2011) p. 845–852.
[39] G. Kresse and J. Furthmüller, Physical Review B **54**, 11169 (1996).
[40] P. E. Blöchl, Physical Review B **50**, 17953 (1994).
[41] G. Kresse and D. Joubert, Physical Review B **59**, 1758 (1999).
[42] M. Dion, H. Rydberg, E. Schröder, D. C. Langreth, and B. I. Lundqvist, Physical Review Letters **92**, 246401 (2004).
[43] K. Berland and P. Hyldgaard, Physical Review B **89**, 035412 (2014).
[44] X. Gonze and C. Lee, Physical Review B **55**, 10355 (1997).
[45] T. Sun, X. Shen, and P. B. Allen, Physical Review B **82**, 224304 (2010).
[46] A. Rohskopf, R. Li, T. Luo, and A. Henry, Modelling and Simulation in Materials Science and Engineering **30**, 045010 (2022).
[47] E. Berger, E. Fransson, F. Eriksson, E. Lindgren, G. Wahnström, T. H. Rod, and P. Erhart, Computer Physics Communications **316**, 109759 (2025).
[48] G. Kemeny, S. D. Mahanti, and T. A. Kaplan, Physical Review B **34**, 6288 (1986).
[49] L. Dabelow, S. Bo, and R. Eichhorn, Physical Review X **9**, 021009 (2019).

ACKNOWLEDGMENTS

FE, EF, and PE acknowledge funding from the Swedish Research Council (Nos. 2020-04935 and 2025-03999) and the Knut and Alice Wallenberg Foundation (No. 2024.0042). RMG and YQ acknowledge support from the Swedish Research Council (VR Starting Grant No. 2022-03350), the Olle Engkvist Foundation (No. 229-0443), the Royal Physiographic Society in Lund (Horisont), the Knut and Alice Wallenberg Foundation (No. 2023.0087), and Chalmers University of Technology, via the Department of Physics and the Areas of Advance Nano and Materials. The computations were enabled by resources provided by the National Academic Infrastructure for Supercomputing in Sweden (NAISS) at PDC, C3SE, and NSC, partially funded by the Swedish Research Council through grant agreement no. 2022-06725, and the Berzelius resource provided by the Knut and Alice Wallenberg Foundation at NSC.

Supporting Information

Non-Markovian heat production in ultrafast phonon dynamics

Fredrik Eriksson,[1] Yulong Qiao,[1] Erik Fransson,[1] R. Matthias Geilhufe,[1] and Paul Erhart[1,2]

[1] Chalmers University of Technology, Department of Physics, 41926 Gothenburg, Sweden
[2] Wallenberg Initiative Materials Science for Sustainability, Chalmers University of Technology, 41926 Gothenburg, Sweden

Contents

Supplementary Notes

Supplementary Note 1: Strontium titanate ($SrTiO_3$)

SrTiO3 (STO) provides a prototypical platform for studying the ultrafast thermodynamics of lattice instabilities. At ambient temperature and pressure, it crystallizes in a cubic perovskite structure ($Pm\bar{3}m$), while upon cooling around 105 K it undergoes a structural phase transition to a tetragonal phase ($I4/mcm$) [1–3]. This transition is driven by a soft phonon mode associated with out-of-phase rotations of the oxygen octahedra. In the harmonic phonon dispersion of the cubic phase, this instability manifests itself as a zone-boundary mode at the R point with an imaginary frequency, reflecting the tendency toward octahedral tilting already at zero temperature (Figure 1b). The presence of such a lattice instability at the harmonic level highlights the strongly anharmonic nature of the lattice dynamics in STO.

In addition to this zone-boundary instability, STO hosts several low-energy optical phonons at the Brillouin-zone center. The ferroelectric soft mode that is the focus of the present work appears as the lowest of four zone-center modes in the phonon dispersion (mode A in Figure 1b). Its frequency exhibits a pronounced temperature dependence, varying from approximately 0 THz close to zero temperature to about 2.7 THz at room temperature [4], characteristic of soft-mode behavior. This tunability is exploited in state-of-the-art pump–probe experiments to achieve resonance between the ferroelectric mode and THz laser pulses through temperature control of the material. While the softening of mode A upon cooling signals an incipient ferroelectric instability, long-range ferroelectric order is suppressed by quantum nuclear effects, stabilizing a quantum paraelectric phase in the $T \to 0$ limit [5]. This fluctuation-driven stabilization underscores the central role of fluctuations in governing the dynamics and thermodynamics of the ferroelectric soft mode.

Capturing this interplay between lattice instabilities, fluctuations, and dissipation requires a description that goes beyond harmonic or weakly anharmonic models. In the present study, we therefore employ a MLIP based on the neuroevolution potential (NEP) framework (Supp. Note 2) as an efficient emulator for density functional theory (DFT) calculations (Supp. Note 4), using the van-der-Waals density functional with consistent exchange. While this functional does not predict the ferroelectric mode to be unstable in the harmonic limit, the mode remains soft (Figure S3). We note that the corresponding energy landscape is sensitive to strain as well as to the treatment of exchange–correlation, leading to uncertainties in transition temperatures [6]. Nevertheless, the essential lattice dynamics and mode couplings relevant for the present work are well captured.

Supplementary Note 2: Training of the machine-learned interatomic potential

We trained a MLIP within the NEP framework. For this purpose, we used the GPUMD [7, 8] and CALORINE packages [9]. The NEP architecture employs a shallow neural network in which the local atomic environment is represented by the descriptor introduced in Refs. 7, 10. The radial and angular cutoffs were set to 8 Å and 4 Å, respectively. The descriptor was parameterized with $n_{\max} = (8, 6)$ and $l_{\max} = (4, 0)$, and the hidden layer dimension was chosen as 40. Both the L_1 and L_2 norms of the parameter vector were regularized with $\lambda_1 = \lambda_2 = 0.1$. Training was performed using the separable natural evolution strategy (SNES) algorithm [11] with energies, forces, and virials obtained from DFT calculations.

The model was trained using the iterative strategy described in Ref. 12. The training set comprised cubic and tetragonal primitive cells at different volumes and cell shapes, as well as molecular dynamics (MD) snapshots from $4 \times 4 \times 4$ (320 atoms) supercells at temperatures ranging from 0 K to 500 K. In addition, structures with imposed tilt modes and ferroelectric distortions were included. The MD structures were generated using a preliminary NEP model and selected based on model uncertainty, estimated from an ensemble of independently trained models [12]. The final NEP model was trained on the complete dataset accumulated during this iterative refinement procedure.

Supplementary Note 3: Validation of the MLIP model

The accuracy of the NEP model is illustrated in the parity plots (Figure S1). The root-mean-square errors (RMSEs) for the validation set are 1.3 meV/atom, 82 meV/Å, and 14 meV/atom for energies, forces, and virials, respectively.

Additionally, we validated the model by computing the harmonic phonon dispersion for several lattice parameters and comparing the results with DFT calculations (Figure S2). In these calculations, we employed $4 \times 4 \times 4$ supercells (320 atoms) and the PHONOPY package [13]. The agreement between the NEP predictions and the DFT results is very good, notably this also applies to the unstable modes with strong anharmonicity.

Supplementary Note 4: Density functional theory calculations

The reference energies, forces, and virials used for training the MLIP model were obtained from DFT calculations employing the van der Waals density functional with consistent exchange (vdW-DF-cx) [14, 15] and the projector augmented wave method [16, 17], as implemented in the Vienna Ab initio Simulation Package [18]. An energy cutoff of 520 eV was used for the plane-wave basis. The Brillouin zone was sampled using a Monkhorst–Pack grid with a maximum k-point spacing of 0.19/Å. The Born effective charges (BECs) of the primitive cubic structure were computed using density functional perturbation theory with the PBEsol functional [19].

Supplementary Note 5: Molecular dynamics simulations

All MD simulations were performed using GPUMD [7, 20]. A timestep of 1 fs and an equilibration time of 50 ps were used throughout.

The simulations were carried out in supercells of size $12 \times 12 \times 12$ cubic primitive cells (8640 atoms). The time-dependent mode coordinates $Q_\lambda(t)$ for a phonon mode $\lambda = (\mathbf{k}, n)$ were obtained by projecting each MD snapshot onto the corresponding phonon eigenvectors [21, 22] as implemented in the DYNASOR package [23]. In particular, for the modes at the Γ point ($\mathbf{k} = \mathbf{0}$), we compute

$$Q_\lambda(t) = \frac{1}{\sqrt{N_c}} \sum_{\nu,\alpha} \sqrt{m_\nu} \mathbf{e}^\lambda_{\nu\alpha} \tau_{\nu\alpha}(t), \tag{1}$$

where N_c denotes the number of unit cells and $\mathbf{e}^\lambda_{\nu\alpha}$ is the normalized eigenvector. The ferroelectric soft mode A corresponds to $n = 1$. Here, ν and α label the atomic species and Cartesian directions, respectively, m_ν is the atomic mass, and $\tau_{\nu\alpha}(t)$ is the Γ-point Fourier component of the atomic displacement. The mass-weighted coordinate Q_λ therefore has units of $\sqrt{\text{Da}}$ Å. The mode coordinates for all other phonon modes were obtained analogously. Results from the non-equilibrium simulations were ensemble averaged over 1000 independent realizations.

Supplementary Note 6: Extraction of the stochastic force from MD

The full character of the stochastic force $\xi(t)$ in the Langevin model can be investigated from MD simulations. To this end, we write the total force, $F_{\text{tot}}(t)$, acting on a mode coordinate, $Q_\lambda(t)$, as a sum over a harmonic force, a damping term, and a stochastic force, in the Langevin equation

$$F_{\text{tot}}(t) = -\omega^2 Q_\lambda(t) - \gamma \dot{Q}_\lambda(t) + \xi(t), \tag{2}$$

where ω is the frequency, γ is the damping, $Q_\lambda(t)$ and $\dot{Q}_\lambda(t)$ are the mode coordinate and generalized velocity (or momentum), respectively. The total mode force, $F_{\text{tot}}(t)$, can be recorded from MD simulation by projecting the atomic forces onto the phonon eigenmode. $Q_\lambda(t)$ and $\dot{Q}_\lambda(t)$ are obtained in the same fashion. Next, the frequency, ω, and damping, γ, are obtained by fitting the MD data to Eq. (2) excluding the stochastic force $\xi(t)$ term. Once ω and γ are known, the stochastic force $\xi(t)$ and its autocorrelation function $\langle \xi(t)\xi(t_0) \rangle$ can be computed along the MD trajectory. This is done in equilibrium NVE simulations (no laser active) at 300 K and the results are shown in Figure S5. We run simulations of length 5 ns to compute $\langle \xi(\tau)\xi(t_0) \rangle$.

Supplementary Note 7: Mode potential energy landscapes

Next, we inspect at the coupling of the potential energy landscapes between modes A, B, C, and D. Figure S6 shows the energy landscape for modes B, C, and D for different amplitudes of mode A, Q_A. This demonstrates that when mode A is activated, $Q_\text{A} \neq 0$, the energy landscapes for the other modes change, representing mode–mode coupling. For Mode B, the energy landscape changes drastically when mode A is activated, indicating strong coupling. Mode C is almost unaffected by mode A, consistent with A and C belonging to different irreducible representations (Table S1). Finally, the effect of mode A activation on mode D is notable but smaller than for mode B, indicating intermediate coupling.

Supplementary Note 8: Mode effective charge

In line with cubic symmetry, we choose the soft mode to be excited along the Cartesian x-direction, where the components of the normalized eigenvector $\mathbf{e}^\text{A}_{\nu\alpha}$ are given by

$$e^\text{A}_{\text{Sr}\,x} = 0.801 \qquad e^\text{A}_{\text{O}^{(1)}\,x} = e^\text{A}_{\text{O}^{(2)}\,x} = -0.219 \qquad e^\text{A}_{\nu,y} = 0$$
$$e^\text{A}_{\text{Ti}\,x} = 0.469 \qquad e^\text{A}_{\text{O}^{(3)}\,x} = -0.174 \qquad e^\text{A}_{\nu,z} = 0$$

The Born effective charge tensor $Z^*_{\nu\alpha\beta}$ is given by

Sr	2.55229	0	0
	0	2.55216	0
	0	0	2.55223
Ti	7.41265	0	0
	0	7.41263	0
	0	0	7.41265
O_{xy}	−2.04370	0	0
	0	−2.04363	0
	0	0	−5.87752
O_{xz}	−2.04370	0	0
	0	−5.87752	0
	0	0	−2.04368
O_{yz}	−5.87754	0	0
	0	−2.04363	0
	0	0	−2.04368

The mode effective charge including the mass factor is calculated as

$$\widetilde{Z}^*_\beta = \sum_{\nu,\alpha} e^{\mathrm{A}}_{\nu\alpha} \frac{Z^*_{\nu\alpha\beta}}{\sqrt{m_\nu}} = \sum_{\nu} e^{\mathrm{A}}_{\nu x} \frac{Z^*_{\nu xx}}{\sqrt{m_\nu}} = 1.2022. \tag{3}$$

The corresponding units are $\mathrm{e}^+/\sqrt{\mathrm{Da}}$.

In contrast, the mode effective charge without the mass factor is given by

$$\widetilde{Z}^*_\beta = \sum_{\nu,\alpha} e^{\mathrm{A}}_{\nu\alpha} Z^*_{\nu\alpha\beta} = \sum_{\nu} e^{\mathrm{A}}_{\nu x} Z^*_{\nu xx} = 7.4577, \tag{4}$$

with unit e^+.

Supplementary Note 9: Microscopic model of the stochastic thermodynamics

In this section, we employ the classical version of the Claderia-Leggett model [24–26] to derive the generalized Langevin equation of the soft mode in the main text, and analyze the Markovianity and the impact of the ultrafast driving on dynamics in the Fourier domain.

System and equations of motion

Consider a system of interacting phonons modeled as coupled classical harmonic oscillators. The Lagrangian for this system is given by:

$$\mathcal{L} = \frac{\dot{Q}^2_{\mathrm{A}}}{2} - \frac{\omega^2_{\mathrm{A}}}{2} Q^2_{\mathrm{A}} + F_{\mathrm{L}}(t) Q_{\mathrm{A}} + \sum_{i=1} \left[\frac{\dot{Q}^2_i}{2} - \frac{\omega^2_i}{2} \left(Q_i - \frac{\kappa_i}{\omega^2_i} Q_{\mathrm{A}} \right)^2 \right], \tag{5}$$

where Q_{A} represents the phonon mode of interest with frequency ω_{A}, and Q_i corresponds to environmental modes with frequencies ω_i. The i is a two-component index $(\lambda, \mathbf{k})$ with λ and $\mathbf{k}$ being band index and wavevector, respectively. $F_{\mathrm{L}}(t)$ denotes the external driving force referred to in the main text, which, for a laser excitation, is determined by the mode effective charge and the screened electric field. The coupling between Q_{A} and environmental modes is mediated by second-order phonon-phonon interactions with strength κ_i.

The Euler-Lagrange equations yield the equations of motion

$$\frac{d}{dt} \frac{\partial \mathcal{L}}{\partial \dot{Q}_j} - \frac{\partial \mathcal{L}}{\partial Q_j} = 0 \quad (j = 0, 1, 2, \cdots), \tag{6}$$

resulting in the coupled equations

$$\ddot{Q}_{\mathrm{A}} + \omega^2_{\mathrm{A}} Q_{\mathrm{A}} + \sum_i \frac{\kappa^2_i}{\omega^2_i} Q_{\mathrm{A}} = F_{\mathrm{L}}(t) + \sum_i \kappa_i Q_i, \tag{7}$$

$$\ddot{Q}_i + \omega^2_i Q_i = \kappa_i Q_{\mathrm{A}}, \quad (i = 1, 2, \cdots). \tag{8}$$

The formal solution to Eq. (8) can be expressed as

$$Q_i(t) = A_i \sin(\omega_i t) + B_i \cos(\omega_i t) + \kappa_i \int_{t_0}^{t} \frac{\sin[\omega_i(t-s)]}{\omega_i} Q_{\mathrm{A}}(s) ds, \tag{9}$$

with initial conditions $B_i = Q_i(t_0)$ and $A_i = \dot{Q}_i(t_0)/\omega_i$. Applying integration by parts, allows us to rewrite Eq. (9)) as

$$\begin{aligned} Q_i(t) = A_i \sin(\omega_i t) + B_i \cos(\omega_i t) + \frac{\kappa_i}{\omega_i^2} Q_{\mathrm{A}}(t) \\ - \frac{\kappa_i}{\omega_i^2} \cos(\omega_i t) Q_{\mathrm{A}}(t_0) - \frac{\kappa_i}{\omega_i^2} \int_{t_0}^{t} \cos[\omega_i(t-s)] \dot{Q}_{\mathrm{A}}(s) ds. \end{aligned} \tag{10}$$

Substituting Eq. (10) into Eq. (7) and setting $Q_{\mathrm{A}}(t_0) = 0$, we obtain the following reduced equation for Q_{A},

$$\ddot{Q}_{\mathrm{A}} + \omega_{\mathrm{A}}^2 Q_{\mathrm{A}} + \sum_i \frac{\kappa_i^2}{\omega_i^2} \int_{t_0}^{t} \cos[\omega_i(t-s)] \dot{Q}_{\mathrm{A}}(s) ds = F_{\mathrm{L}}(t) + \sum_i \kappa_i \left[A_i \sin(\omega_i t) + B_i \cos(\omega_i t) \right].$$

By explicitly introducing the spectral density of the bath $J(\omega)$, which is defined as

$$J(\omega) = \sum_i \frac{\kappa_i^2}{\omega_i} \delta(\omega - \omega_i). \tag{11}$$

If the density of the state of the bath $D(\omega)$ is known, $J(\omega)$ can be expressed as

$$J(\omega) = D(\omega) \frac{\kappa^2(\omega)}{\omega}. \tag{12}$$

With the definition Eq. (11) we have

$$\ddot{Q}_{\mathrm{A}} + \omega_{\mathrm{A}}^2 Q_{\mathrm{A}} + \int_{t_0}^{t} f(t-s) \dot{Q}_{\mathrm{A}}(s) ds = F_{\mathrm{L}}(t) + \xi(t), \tag{13}$$

where

$$\begin{aligned} \xi(t) &= \sum_i \kappa_i \left[A_i \sin(\omega_i t) + B_i \cos(\omega_i t) \right] \\ &= \sum_i \frac{\kappa_i}{\omega_i} \left[\sin(\omega_i t) \dot{Q}_i(t_0) + \omega_i \cos(\omega_i t) Q_i(t_0) \right] \end{aligned} \tag{14}$$

represents noise originating from the initial conditions of environmental modes and the nonlocal friction kernel

$$f(t) = \int_0^{\infty} \mathrm{d}\omega \frac{J(\omega)}{\omega} \cos(\omega t), \tag{15}$$

characterizes non-Markovian dynamics.

Assuming Gaussian distributed initial positions $Q_i(t_0)$ and velocities $\dot{Q}_i(t_0)$ of environmental modes with zero ensemble averages, we find

$$\langle \xi(t) \rangle = \sum_i \frac{\kappa_i}{\omega_i} \left[\sin(\omega_i t) \langle \dot{Q}_i(t_0) \rangle + \omega_i \cos(\omega_i t) \langle Q_i(t_0) \rangle \right] = 0. \tag{16}$$

The noise correlation function is derived as

$$\begin{aligned} \langle \xi(t) \xi(t') \rangle &= \sum_i \frac{\kappa_i^2}{\omega_i^2} \left[\sin(\omega_i t) \sin(\omega_i t') \langle \dot{Q}_i^2(t_0) \rangle + \cos(\omega_i t) \cos(\omega_i t') \langle \omega_i^2 Q_i^2(t_0) \rangle \right] \\ &= k_{\mathrm{B}} T \int_0^{\infty} \mathrm{d}\omega \frac{J(\omega)}{\omega} \cos[\omega(t-t')], \end{aligned} \tag{17}$$

where statistical independence between different modes ($\dot{Q}_i(t_0)$ and $Q_i(t_0)$) has been assumed. The third equality assumes as initial condition thermal equilibrium at temperature T (with k_{B} denoting Boltzmann's constant). From (Eq. (17) and Eq. (15) the fluctuation-dissipation theorem reads

$$\langle \xi(t) \xi(t') \rangle = k_{\mathrm{B}} T f(|t-t'|). \tag{18}$$

The Fourier transformation of the noise autocorrelation function $\langle \xi(t)\xi(t_0)\rangle$ is

$$\begin{aligned}\mathcal{F}[\langle \xi(\tau)\xi(t_0)\rangle](\omega) &= k_{\mathrm{B}}T \int_0^\infty \mathrm{d}\omega' \frac{J(\omega')}{\omega'} \int_{-\infty}^\infty \mathrm{d}\tau \cos(\omega'\tau)\mathrm{e}^{-i\omega\tau} \\ &= \pi k_{\mathrm{B}}T \int_{-\infty}^\infty \mathrm{d}\omega' \frac{J(\omega')}{\omega'} \left[\delta(\omega-\omega') + \delta(\omega+\omega')\right] \\ &= \pi k_{\mathrm{B}}T \frac{J(|\omega|)}{|\omega|}. \end{aligned} \tag{19}$$

Impact of external driving on Markovianity

In the Fourier domain, the solution of Eq. (13) by extending t_0 to the remote past reads

$$\widetilde{Q}_{\mathrm{A}}(\omega) = \frac{F_{\mathrm{L}}(\omega) + \tilde{\xi}(\omega)}{\omega_{\mathrm{A}}^2 - \omega^2 + i\omega\tilde{f}(\omega)}, \tag{20}$$

where $F_{\mathrm{L}}(\omega)$ and $\tilde{\xi}(\omega)$ are obtained via standard Fourier transformation

$$F_{\mathrm{L}}(\omega) = \int_{-\infty}^\infty dt\, F_{\mathrm{L}}(t) e^{-i\omega t}, \tag{21}$$

$$\tilde{f}(\omega) = \int_{-\infty}^\infty dt\, f(t) e^{-i\omega t}, \tag{22}$$

$$\tilde{\xi}(\omega) = \int_{-\infty}^\infty dt\, \xi(t) e^{-i\omega t}, \tag{23}$$

Considering Eq. (15), we have

$$\tilde{f}(\omega) \propto \frac{J(|\omega|)}{|\omega|}, \tag{24}$$

while the imaginary part is given by the principal value.

We now define the frequency response function

$$\chi(\omega) = \frac{1}{\omega_{\mathrm{A}}^2 - \omega^2 + i\omega\tilde{f}(\omega)}, \tag{25}$$

the ensemble-averaged response becomes

$$\langle \widetilde{Q}_{\mathrm{A}}(\omega)\rangle = \chi(\omega) F_{\mathrm{L}}(\omega). \tag{26}$$

Hence, the distribution of $F_{\mathrm{L}}(t)$ in the Fourier domain has a fundamental impact on the dynamics. A short pulse (small τ) corresponds to fast driving, yielding a broad $F_{\mathrm{L}}(\omega)$ that excites many frequency components within the effective band of $\chi(\omega)$. In contrast, a long pulse (large τ) corresponds to slow driving, with a narrow spectral distribution that mainly probes the vicinity of ω_A. In this sense, ultrafast driving can serve as a frequency-resolved probe of the system.

Supplementary Tables

Table S1: Zone-center phonon modes in $SrTiO_3$. Frequencies are obtained from MD simulations at 300 K. The irreducible representations (irreps) are obtained from the direct product representation of the five-dimensional permutation representation Γ_p for the point group O_h and the 5 unit cell sites with the vector representation $\Gamma_v = T_{1u}$ [27]. Using GTPack [28], we obtain $\Gamma_p \otimes \Gamma_v \simeq 4T_{1u} \oplus T_{2u}$.

Mode	Frequency (THz)	Damping (THz)	Irreps
A	3.84	0.34	T_{1u}
B	5.26	0.28	T_{1u}
C	7.59	0.33	T_{2u}
D	15.74	0.50	T_{1u}

Supplementary Figures

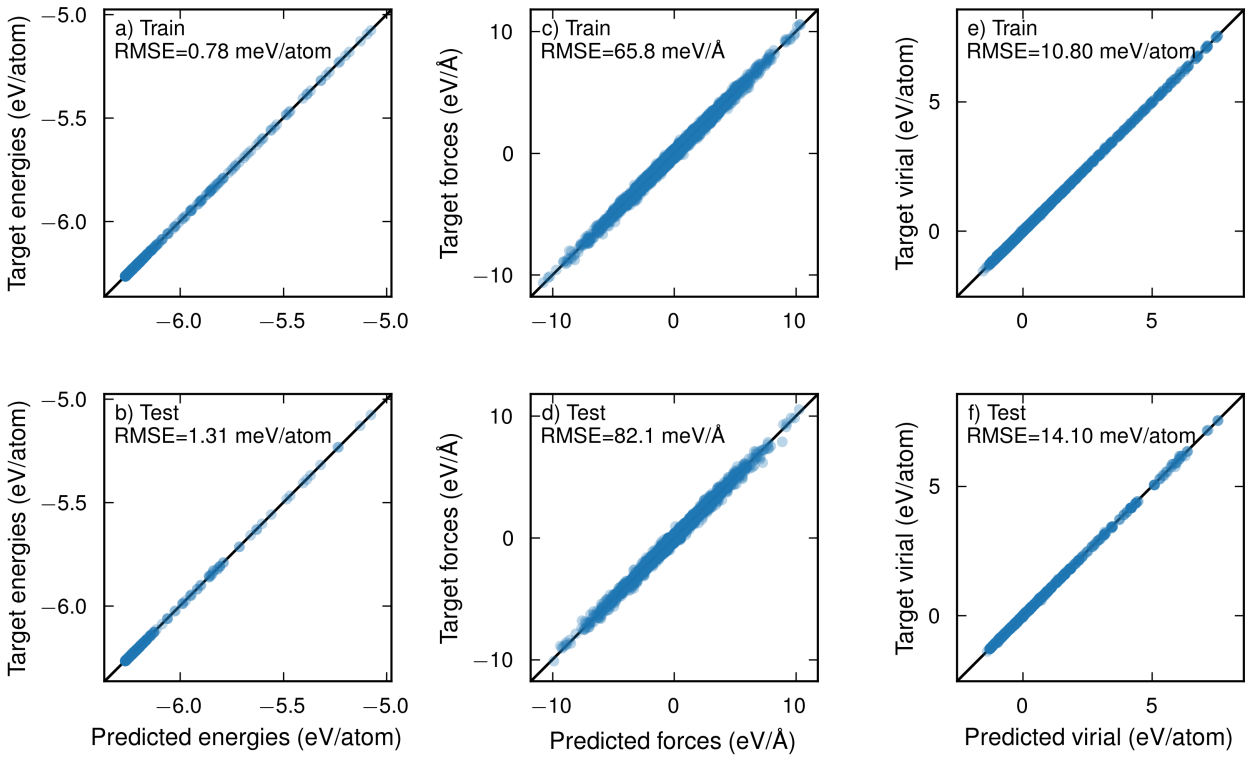

Figure S1: Parity plots for energies, forces, and virials for the training and validation sets comparing the predictions of the NEP model with reference data from DFT calculations.

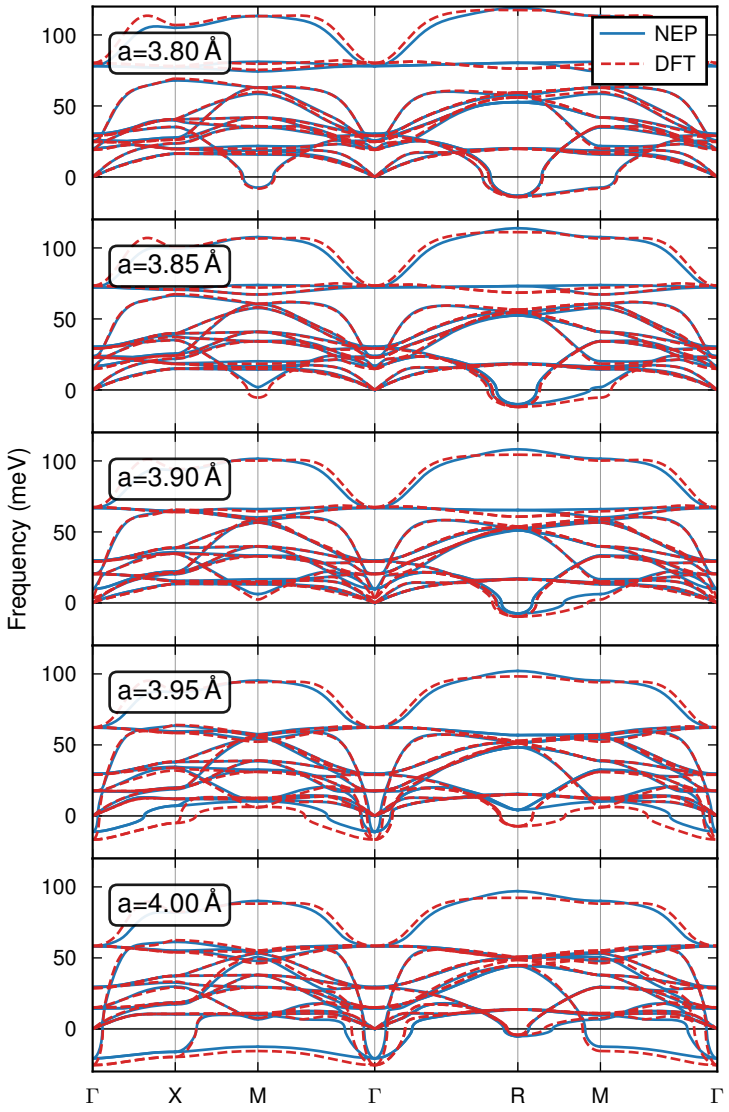

Figure S2: Phonon dispersions for cubic $SrTiO_3$ from DFT and NEP calculations for different lattice parameters.

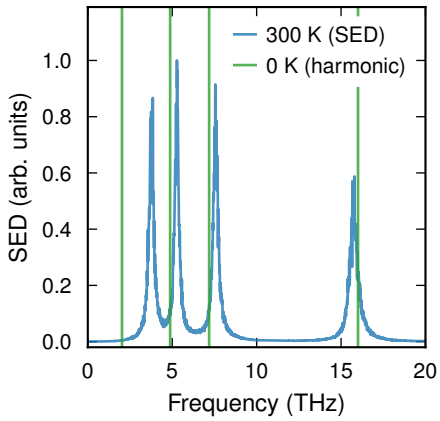

Figure S3: Temperature dependence of Γ-point modes. The vertical lines indicate the frequencies in the harmonic limit (also see Figure S2 and Figure 1b in the main text). The blue lines show the spectral energy density at the Γ-point sampled at 300 K.

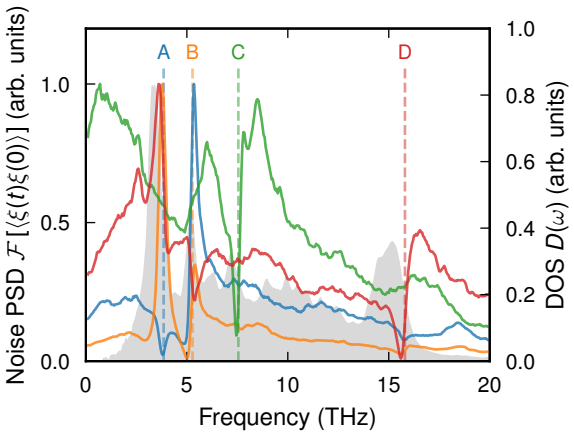

Figure S4: Noise power spectral densitys (PSDs) for Γ-point modes in comparison with the density of states (DOS) (gray filled region). The vertical lines indicate the frequencies at 300 K (see Figure S3).

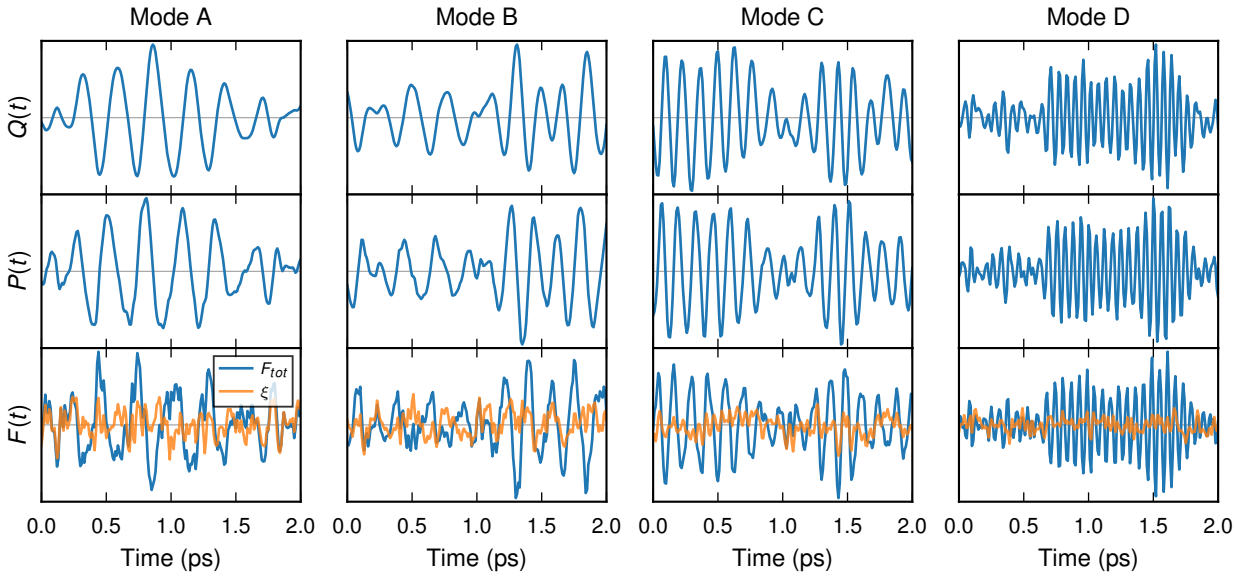

Figure S5: Mode projections along an equilibrium MD simulation for the four zone-center modes (A–D). Here, only a short 2 ps interval is shown to clearly visualize the oscillations in the time signals.

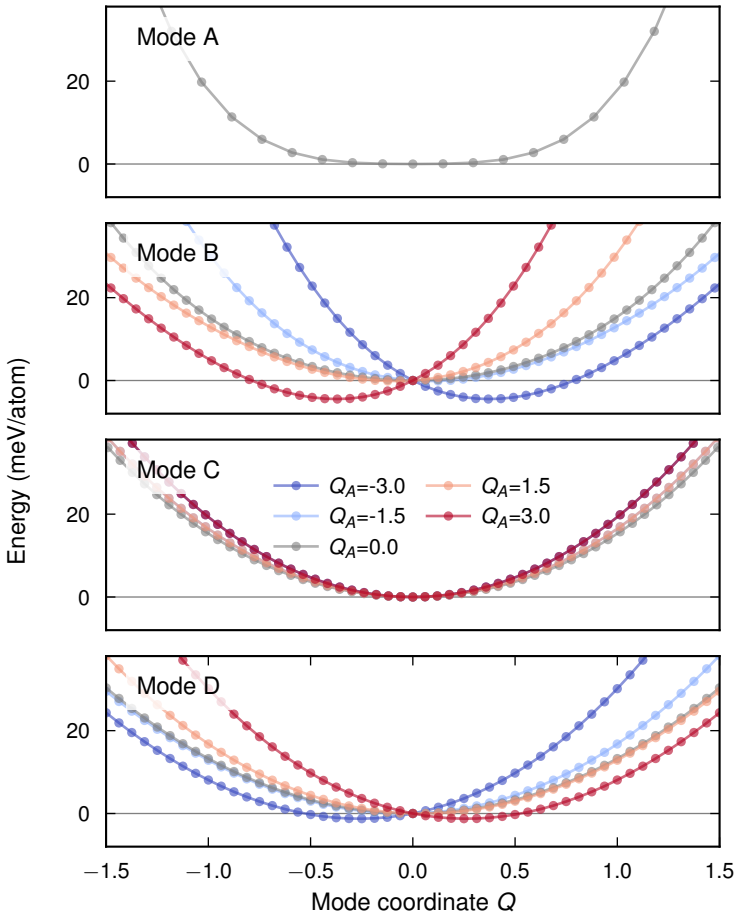

Figure S6: Mode energy landscapes along the mode coordinates for the four zone-center modes (A–D). For modes B, C, and D, the coloring indicates the amplitude set for mode A, Q_A. The energy for modes B, C, and D is shown after subtraction of the energy $E(Q_\mathrm{A})$ (from the top panel).

Supplementary References

[1] P. A. Fleury, J. F. Scott, and J. M. Worlock, *Soft Phonon Modes and the* 110 K *Phase Transition in $SrTiO_3$,* Physical Review Letters **21**, 16 (1968). doi:10.1103/physrevlett.21.16.

[2] R. A. Cowley, *The phase transition of strontium titanate,* Philosophical Transactions of the Royal Society of London. Series A: Mathematical, Physical and Engineering Sciences **354**, 2799 (1996). doi:10.1098/rsta.1996.0130.

[3] M. Holt, M. Sutton, P. Zschack, H. Hong, and T.-C. Chiang, *Dynamic Fluctuations and Static Speckle in Critical X-Ray Scattering from $SrTiO_3$,* Physical Review Letters **98**, 065501 (2007). doi:10.1103/physrevlett.98.065501.

[4] H. Vogt, *Refined treatment of the model of linearly coupled anharmonic oscillators and its application to the temperature dependence of the zone-center soft-mode frequencies of $KTaO_3$ and $SrTiO_3$,* Physical Review B **51**, 8046 (1995). doi:10.1103/PhysRevB.51.8046.

[5] K. A. Müller and H. Burkard, *$SrTiO_3$: An intrinsic quantum paraelectric below* 4 K, Physical Review B **19**, 3593 (1979). doi:10.1103/PhysRevB.19.3593.

[6] C. Verdi, L. Ranalli, C. Franchini, and G. Kresse, *Quantum Paraelectricity and Structural Phase Transitions in Strontium Titanate beyond Density Functional Theory,* Physical Review Materials **7**, L030801 (2023). doi:10.1103/PhysRevMaterials.7.L030801.

[7] Z. Fan, Y. Wang, P. Ying, K. Song, J. Wang, Y. Wang, Z. Zeng, K. Xu, E. Lindgren, J. M. Rahm, A. J. Gabourie, J. Liu, H. Dong, J. Wu, Y. Chen, Z. Zhong, J. Sun, P. Erhart, Y. Su, and T. Ala-Nissila, *GPUMD: A Package for Constructing Accurate Machine-Learned Potentials and Performing Highly Efficient Atomistic Simulations,* The Journal of Chemical Physics **157**, 114801 (2022). doi:10.1063/5.0106617.

[8] K. Xu, H. Bu, S. Pan, E. Lindgren, Y. Wu, Y. Wang, J. Liu, K. Song, B. Xu, Y. Li, T. Hainer, L. Svensson, J. Wiktor, R. Zhao, H. Huang, C. Qian, S. Zhang, Z. Zeng, B. Zhang, B. Tang, Y. Xiao, Z. Yan, J. Shi, Z. Liang, J. Wang, T. Liang, S. Cao, Y. Wang, P. Ying, N. Xu, C. Chen, Y. Zhang, Z. Chen, X. Wu, W. Jiang, E. Berger, Y. Li, S. Chen, A. J. Gabourie, H. Dong, S. Xiong, N. Wei, Y. Chen, J. Xu, F. Ding, Z. Sun, T. Ala-Nissila, A. Harju, J. Zheng, P. Guan, P. Erhart, J. Sun, W. Ouyang, Y. Su, and Z. Fan, *GPUMD 4.0: A high-performance molecular dynamics package for versatile materials simulations with machine-learned potentials,* Materials Genome Engineering Advances **3**, e70028 (2025). doi:doi:10.1002/mgea.70028.

[9] E. Lindgren, M. Rahm, E. Fransson, F. Eriksson, N. Österbacka, Z. Fan, and P. Erhart, *Calorine: A Python Package for Constructing and Sampling Neuroevolution Potential Models,* Journal of Open Source Software **9**, 6264 (2024). doi:10.21105/joss.06264.

[10] K. Song, R. Zhao, J. Liu, Y. Wang, E. Lindgren, Y. Wang, S. Chen, K. Xu, T. Liang, P. Ying, N. Xu, Z. Zhao, J. Shi, J. Wang, S. Lyu, Z. Zeng, S. Liang, H. Dong, L. Sun, Y. Chen, Z. Zhang, W. Guo, P. Qian, J. Sun, P. Erhart, T. Ala-Nissila, Y. Su, and Z. Fan, *General-purpose machine-learned potential for 16 elemental metals and their alloys,* Nature Communications **15**, 10208 (2024). doi:10.1038/s41467-024-54554-x.

[11] T. Schaul, T. Glasmachers, and J. Schmidhuber, *High dimensions and heavy tails for natural evolution strategies,* in *Proceedings of the 13th Annual Conference on Genetic and Evolutionary Computation*, GECCO '11, (New York, NY, USA), 845–852, Association for Computing Machinery, 2011. doi:10.1145/2001576.2001692.

[12] E. Fransson, J. Wiktor, and P. Erhart, *Phase Transitions in Inorganic Halide Perovskites from Machine-Learned Potentials,* The Journal of Physical Chemistry C **127**, 13773 (2023). doi:10.1021/acs.jpcc.3c01542.

[13] A. Togo and I. Tanaka, *First principles phonon calculations in materials science,* Scripta Materialia **108**, 1 (2015). doi:10.1016/j.scriptamat.2015.07.021.

[14] M. Dion, H. Rydberg, E. Schröder, D. C. Langreth, and B. I. Lundqvist, *Van der Waals Density Functional for General Geometries,* Physical Review Letters **92**, 246401 (2004). doi:10.1103/PhysRevLett.92.246401.

[15] K. Berland and P. Hyldgaard, *Exchange functional that tests the robustness of the plasmon description of the van der Waals density functional,* Physical Review B **89**, 035412 (2014). doi:10.1103/PhysRevB.89.035412.

[16] P. E. Blöchl, *Projector augmented-wave method,* Physical Review B **50**, 17953 (1994). doi:10.1103/PhysRevB.50.17953.

[17] G. Kresse and D. Joubert, *From ultrasoft pseudopotentials to the projector augmented-wave method,* Physical Review B **59**, 1758 (1999). doi:10.1103/PhysRevB.59.1758.

[18] G. Kresse and J. Furthmüller, *Efficient iterative schemes for ab initio total-energy calculations using a plane-wave basis set,* Physical Review B **54**, 11169 (1996). doi:10.1103/PhysRevB.54.11169.

[19] J. P. Perdew, A. Ruzsinszky, G. I. Csonka, O. A. Vydrov, G. E. Scuseria, L. A. Constantin, X. Zhou, and K. Burke, *Restoring the Density-Gradient Expansion for Exchange in Solids and Surfaces,* Physical Review Letters **100**, 136406 (2008). doi:10.1103/PhysRevLett.100.136406.

[20] Z. Fan, W. Chen, V. Vierimaa, and A. Harju, *Efficient molecular dynamics simulations with many-body potentials on graphics processing units,* Computer Physics Communications **218**, 10 (2017). doi:10.1016/j.cpc.2017.05.003.

[21] T. Sun, X. Shen, and P. B. Allen, *Phonon quasiparticles and anharmonic perturbation theory tested by molecular dynamics on a model system,* Physical Review B **82**, 224304 (2010). doi:10.1103/PhysRevB.82.224304.

[22] A. Rohskopf, R. Li, T. Luo, and A. Henry, *A computational framework for modeling and simulating vibrational mode dynamics,* Modelling and Simulation in Materials Science and Engineering **30**, 045010 (2022). doi:10.1088/1361-651X/ac5ebb.

[23] E. Berger, E. Fransson, F. Eriksson, E. Lindgren, G. Wahnström, T. H. Rod, and P. Erhart, *Dynasor 2: From Simulation to Experiment Through Correlation Functions,* Computer Physics Communications **316**, 109759 (2025). doi:10.1016/j.cpc.2025.109759.

[24] A. Caldeira and A. Leggett, *Path integral approach to quantum Brownian motion,* Physica A: Statistical Mechanics and its Applications **121**, 587 (1983). doi:10.1016/0378-4371(83)90013-4.

[25] A. Caldeira and A. Leggett, *Quantum tunnelling in a dissipative system,* Annals of Physics **149**, 374 (1983). doi:10.1016/0003-4916(83)90202-6.

[26] I. de Vega and D. Alonso, *Dynamics of non-Markovian open quantum systems,* Reviews of Modern Physics **89**, 015001 (2017). doi:10.1103/RevModPhys.89.015001.

[27] W. Hergert and R. M. Geilhufe, *Group Theory in Solid State Physics and Photonics: Problem Solving with Mathematica* (Wiley-VCH, 2018). ISBN: 978-3-527-41133-7.

[28] R. M. Geilhufe and W. Hergert, *GTPack: A Mathematica Group Theory Package for Application in Solid-State Physics and Photonics,* Frontiers in Physics **6**, 86 (2018). doi:10.3389/fphy.2018.00086.